



Research paper

Ti³⁺ self-doped TiO₂ via facile catalytic reduction over Al(acac)₃ with enhanced photoelectrochemical and photocatalytic activities

Jordan Lee^a, Zhong Li^a, Liangzhu Zhu^b, Songhai Xie^{c,*}, Xiaoli Cui^{a,*}^a Department of Materials Science, Fudan University, Shanghai 200433, China^b Department of Materials Science & Engineering, University of Utah, Salt Lake City, UT, 84112, USA^c Department of Chemistry, Fudan University, Shanghai 200433, China

ARTICLE INFO

Keywords:
 Ti³⁺ self-doped TiO₂
 Synthesis mechanism
 Catalytic reduction
 Photocatalytic
 Photoelectrochemical

ABSTRACT

In this work, we have shown that aluminium acetylacetone (Al(acac)₃) can be used as the catalyst to synthesize Ti³⁺ self-doped TiO₂ (Ti³⁺-TiO₂) by sol-gel method in air. Ti³⁺-TiO₂ can be obtained directly and Al(acac)₃ is removed during the annealing process. Ti³⁺ concentrates in the surface layer of powders, making a homojunction between Ti³⁺-TiO₂ in the surface layer and TiO₂ in the bulk. Based on the scheme of Ziegler-Natta catalysts and the characterization of the sols and gels of samples, the synthesis mechanism of Ti³⁺ is proposed as the combination of steric hindrance effect, Lewis acid-base reaction and crystal field effect and Al(acac)₃ acts as the catalyst in the reaction. Charge generation, charge transport and interface reactions, all of the three crucial strategies of photocatalytic are improved through the self-doped Ti³⁺, resulting in enhanced photocatalytic and photoelectrochemical activities. Compared with the reported methods, this work proposes a simple and novel route for the preparation of Ti³⁺-TiO₂, which would facilitate the preparation and application of TiO₂ photocatalyst.

1. Introduction

Nowadays, with serious environmental problems and rapid demands for renewable energy, the utilizations of solar energy in environment purification and solar energy conversion have been an ideal and meaningful study [1]. TiO₂ is one of the most widely investigated semiconductor photocatalyst due to its advantages of chemical stability, strong redox capacity, nontoxicity and extensive source [2]. However, the wide band gap of anatase TiO₂ (3.2 eV) and high recombination rate of electrons and holes make the utilizations of TiO₂ non-competitive to conventional environment materials. Doping with Ti³⁺ to modify TiO₂ has become a research hotspot since both light absorbance and charge separation can be improved by Ti³⁺, which can also narrow the band gap and enhance electrical conductivity [3]. Meanwhile, this strategy does not introduce new recombination centers or thermodynamic instability as impurity atom or ions doping [4].

Numerous efforts are currently being devoted for preparation of Ti³⁺-TiO₂ samples [5–14]. The reported synthesis approaches can be divided into three categories: reduction of Ti⁴⁺ source [5–9], growth of Ti³⁺ source under protective gas [10,11] and oxidation of low-valence Ti source [12–14].

Reduction is the most widely used method in Ti³⁺-TiO₂ preparation

[5–9]. For example, Fang et al. [5] fabricated Ti³⁺-TiO₂ via sol-gel by using tetrabutyl orthotitanate (TBOT) as Ti source and NaBH₄ as reducer. The photocatalytic activity was improved owing to enhanced light absorption. Zheng et al. [6] generated Ti³⁺-TiO₂ by hydrothermal method, using TiCl₄ as Ti source and Zn powder as reducer. The excess Zn in TiO₂ could also suppress the oxidation of Ti³⁺ in air. Wang et al. [7] annealed TiOF₂ films at normal atmosphere to produced TiO₂ nanosheet film with bulk/surface defects. Strong reducers, such as NaBH₄ and active metals, could fabricate Ti³⁺-TiO₂ in air, but specific storage condition should be maintained to avoid oxidation-induced failure. Recently, Jiang et al. [8] presented an oleic acid-assisted solvothermal process for fabricating Ti³⁺-TiO₂ on the basis of carbonization of oleic acid under inert gas at 500–900 °C. Saputera et al. [9] obtained blue Ti³⁺-TiO₂ at 500 °C under NO and CO respectively while Lin et al. [10] produced Ti³⁺-TiO₂ nanowires at 800 °C by Al powder under vacuum. In these processes, isolation of air and high temperature may need extra requirements of equipment.

By applying both Ti³⁺ and Ti⁴⁺ sources, Ti³⁺-TiO₂ can also be obtained [10,11]. Recently, Zhou et al. [11] used TiCl₃ and titanium isopropoxide to synthesize Ti³⁺ self-doped anatase-rutile mixed TiO₂ by hydrothermal method under argon atmosphere. No Ti³⁺ peaks were identified in XPS spectra but a strong ESR signal of 1.94 was observed,

* Corresponding authors.

E-mail addresses: shxie@fudan.edu.cn (S. Xie), xiaolicui@fudan.edu.cn (X. Cui).

indicating that Ti^{3+} lies in the bulk of the samples. Hamdy et al. [12] heated commercial anatase TiO_2 and Ti_2O_3 under static gas at 300–900 °C to obtain $\text{Ti}^{3+}\text{-TiO}_2$, they found that its photocatalytic reactivity is twofold larger than that of P25 in the photodegradation of methylene blue.

$\text{Ti}^{3+}\text{-TiO}_2$ can also be prepared from the oxidation of low-valence Ti source, such as metal Ti and TiH_2 [12–14]. For example, Liu et al. prepared Ti^{3+} self-doped TiO_{2-x} anatase nanoparticles via oxidation of TiH_2 in H_2O_2 [13–15]. Besides, by employing both Ti powder and TBOT as precursors and hydrofluoric acid as solvent, Cai et al. fabricated $\text{Ti}^{3+}\text{-TiO}_2$ nanosheet through a hydrothermal method at 200 °C [16]. The highest photocatalytic activity was achieved when the molar ratio of metal Ti to TBOT reaches 1:20. The oxidation of low-valence Ti source has the advantage of fabricating $\text{Ti}^{3+}\text{-TiO}_2$ sample in air, which is beneficial to simplify the equipment.

In our recent study, we prepared Ti^{3+} self-doped TiO_2 microspheres through selective etching the composite $\text{Al}(\text{acac})_3\text{/Al-TiO}_2$, which was synthesized via facile flame thermal method [17]. $\text{Al}(\text{acac})_3$ has been demonstrated as a special reagent in $\text{Ti}^{3+}\text{-TiO}_2$ synthesis process. It is well known that $\text{Al}(\text{acac})_3$ is a stable reagent in air and we are highly interested in whether $\text{Al}(\text{acac})_3$ could help to synthesize $\text{Ti}^{3+}\text{-TiO}_2$ by a general way such as a sol–gel process, which have not been investigated so far. In this work, Ti^{3+} heavily self-doped TiO_2 photocatalyst is obtained via sol–gel approach in air with the assistance of $\text{Al}(\text{acac})_3$ and it acts as the catalyst in this reaction. The composition of TBOT and $\text{Al}(\text{acac})_3$ is similar to the precursor of Zielger-Natta catalytic because –OH from hydrolyzing intermediate of TBOT is nucleophilic as –Cl from TiCl_4 while –acac from $\text{Al}(\text{acac})_3$ is electrophilic as ($\text{i-C}_4\text{H}_9$) from $\text{Al}(\text{i-C}_4\text{H}_9)_3$. It is also found that Ti^{3+} is not doped uniformly in the samples, with a homojunction between $\text{Ti}^{3+}\text{-TiO}_2$ in the surface layer and mostly TiO_2 in the bulk. Enhanced photoelectrochemical response and photocatalytic activities are demonstrated for the resulted samples on account of wider light absorbance, quicker charge transport and faster interface reaction. By the reference of the scheme of Zielger-Natta catalysts and the characterizations of the sols and gels of samples, the formation mechanism of Ti^{3+} is proposed as a bimetallic radical process through steric hindrance effect, Lewis acid-base reaction and crystal field effect.

2. Materials and methods

2.1. Synthesis of samples

All the reagents were obtained from Sinopharm Chemical Reagent Co. Ltd and employed without any further purification. Briefly, 6 mL tetrabutyl orthotitanate (98%, TBOT), 24 mL absolute ethanol (AR), 1.9 mL acetylacetone (AR, Hacac) and a certain amount of aluminium acetylacetone (98%, $\text{Al}(\text{acac})_3$) were mixed and stirred for 1 h to obtain solution A while solution B consisted of 30 mL absolute ethanol and 3.5 mL H_2O . Solution B was dropwise added into solution A by titration funnel under magnetic stirring. Afterwards, the mixed solution was aged for 24 h to form a sol.

The as-prepared sols were dried at 80 °C under an infrared lamp, followed by annealing at 350 °C in air for 2 h to remove $\text{Al}(\text{acac})_3$ and synthesize the desired $\text{Ti}^{3+}\text{-TiO}_2$ powders directly. Samples with different ratios of Ti^{3+} were signed as X- TiO_2 in which X represented the molar percentage of $\text{Al}(\text{acac})_3$ to TBOT in the precursor. To study the electrochemical property of the samples, the corresponding electrodes of samples were fabricated by spinning the sols on the 7 × 8 mm² fluorine-doped tin oxide (FTO) conducting glasses followed by the same annealing treatment.

For comparison, the undoped TiO_2 (Sample 0- TiO_2) were prepared through the same procedures without the addition of $\text{Al}(\text{acac})_3$.

2.2. Characterizations

X-ray diffraction (XRD) was employed to examine the crystalline structure of the photocatalyst on a Bruker D/8 advanced diffractometer using $\text{Cu K}\alpha$ radiation. Ti^{3+} was analyzed by Electron Spin Resonance (ESR) on a Bruker EMX-8/2.7 at X-bond microwave at 100 K. X-ray photoelectron spectroscopy (XPS) was conducted with a RBD upgrated PHI-5000C ESCA system, which was adjusted by the peak of C1s at 284.6 eV. High resolution transmission electron microscopy (HRTEM) image and energy-dispersive X-ray spectrum (EDS) were taken by a Tecnai G2 F20 S-Twin FE-TEM. N_2 adsorption-desorption isotherms were characterized by a Tristar II 3020 surface area analyzer. UV–vis diffused reflectance spectroscopy (DRS) was obtained by a UV-3150 UV–vis spectrophotometer with BaSO_4 sample disk as the background. Fourier transform infrared (FT-IR) spectra were recorded on a Nicolet Nexus spectrometer with KBr pellets.

2.3. Photoelectrochemical and photocatalytic activities measurements

Photoelectrochemical measurements were performed on a three-electrode cell, with Pt plate as counter electrode, saturated calomel electrode (SCE) as reference electrode, the as-prepared corresponding electrodes as working electrode and 0.5 M Na_2SO_4 solution as electrolyte. The electrochemical impedance spectroscopy (EIS) and Mott-Schottky curves (MS) were implemented on a PARSTAT 4000 Potentiostat/Galvanostat EIS analyzer. The frequency of EIS ranged from 100,000 Hz to 0.02 Hz and MS was scanned at 5 mV/s from –1.5 V to 1.5 V (vs. SCE) at 1000 Hz. Transient photocurrent was measured by a CHI 660A electrochemical workstation under the illumination of simulated solar irradiation. The simulated solar irradiation was constructed by a CHF-XM35 Xenon lamp whose infrared wavelengths were filtered by a quartz water channel and the intensity of the UV–vis light was 84.0 mW/cm².

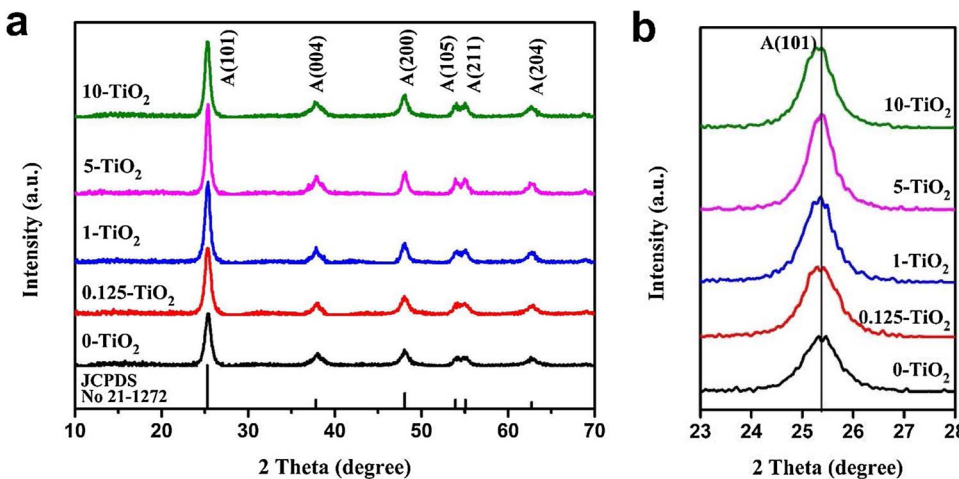
Photocatalytic activity measurements were evaluated by the photodegradation of methylene blue (MB) under simulated solar irradiation in a XPA-7 photochemical reactor at 25 °C. Typically, 10 mg samples were dispersed into 10 mL MB solution (5 mg/L) respectively in each quartz tube by ultrasonic treatment. The adsorption-desorption equilibrium was achieved before degradation through stirring the solution in dark for 2 h. During the photocatalytic reaction, all samples were irradiated simultaneously under spinning and magnetic stirring condition. Every 20 min, the concentration of MB solution was measured on a UV-2300 UV–vis absorption spectroscopy.

3. Results and discussion

3.1. Characterization of samples

Fig. 1a depicts the XRD patterns of samples prepared by using different amount of $\text{Al}(\text{acac})_3$. All diffraction peaks are well ascribed to anatase TiO_2 (JCPDS No. 21-1272) and the crystallinity of powders maintains high even though the molar ratio of Al to Ti reaches 10%. Fig. 1b shows the enlarged (101) XRD peaks of the samples, almost no shift can be observed, indicating that the bulk [18] of the as-prepared powders is composed of TiO_2 .

The existence of Ti^{3+} is detected by ESR and Ti2p XPS spectra, as shown in Fig. 2. ESR is especially suitable to detect the existence of Ti^{3+} for its high sensitivity to species which contain unpaired electrons. As shown in Fig. 2a, the g-value of the signals equals 2.002, which is ascribed to the g-value of surface oxygen vacancies [7,19,20]. With the increasing amount of $\text{Al}(\text{acac})_3$ in the precursors, the intensity of ESR signals also becomes stronger, implying that the content of Ti^{3+} increases accordingly. For the undoped TiO_2 sample, almost no ESR signal can be detected owing to the shortage of unpaired electrons. Ti2p XPS spectra disclose the chemical environment of Ti as depicted in Fig. 2b–d. For undoped TiO_2 sample (Fig. 2b), the Ti2p_{3/2} and Ti2p_{1/2}



core level, 458.4 eV and 464.0 eV, should be attributed to Ti-O-Ti bond [21]. The peak of Ti2p_{3/2} shifts sharply to 457.3 eV for Sample 1-TiO₂ (Fig. 2c) and 457.0 eV for Sample 10-TiO₂ (Fig. 2d), reconfirming the presence of Ti³⁺ in the samples [22]. It is worth noting that the peak intensity is associated with Ti³⁺ is larger than that of Ti⁴⁺, as shown in Fig. 2c-d, implying that Ti³⁺ is heavily doped in the surface layer in the resultant samples. The possibility that the samples are Al doped TiO₂ is excluded by considering the following three aspects. One is that no signal is ascribed to Al element in the survey spectra of Ti³⁺-TiO₂, as shown in Fig. S1. Another is that the binding energy of Ti2p electron of Al doped TiO₂ ought to be larger than TiO₂ [23], which is just opposite

to the variation of the experimental results that is depicted in Fig. 2b-d. The third is that ESR signal of Al doped TiO₂ consists a pair of sextuplets because Al has a nuclear spin of I = 5/2 [24], which is not observed in the ESR results of the as-prepared samples (spectra in Fig. 2a).

Through the combination of the XRD patterns and XPS spectra, the irregular particles, as shown in Fig. S2, are considered as composites of Ti³⁺ heavily doped TiO₂ in the surface layer and undoped TiO₂ in the bulk through the following apagogical discussions. It is well known that XPS is a technology of surface analysis (< 10 nm [25]) while XRD characterizes the bulk of materials (~2 μm [16]). If Ti³⁺ distributes uniformly, XRD patterns would be ascribed to Magnéti phase TiO_{2-x}

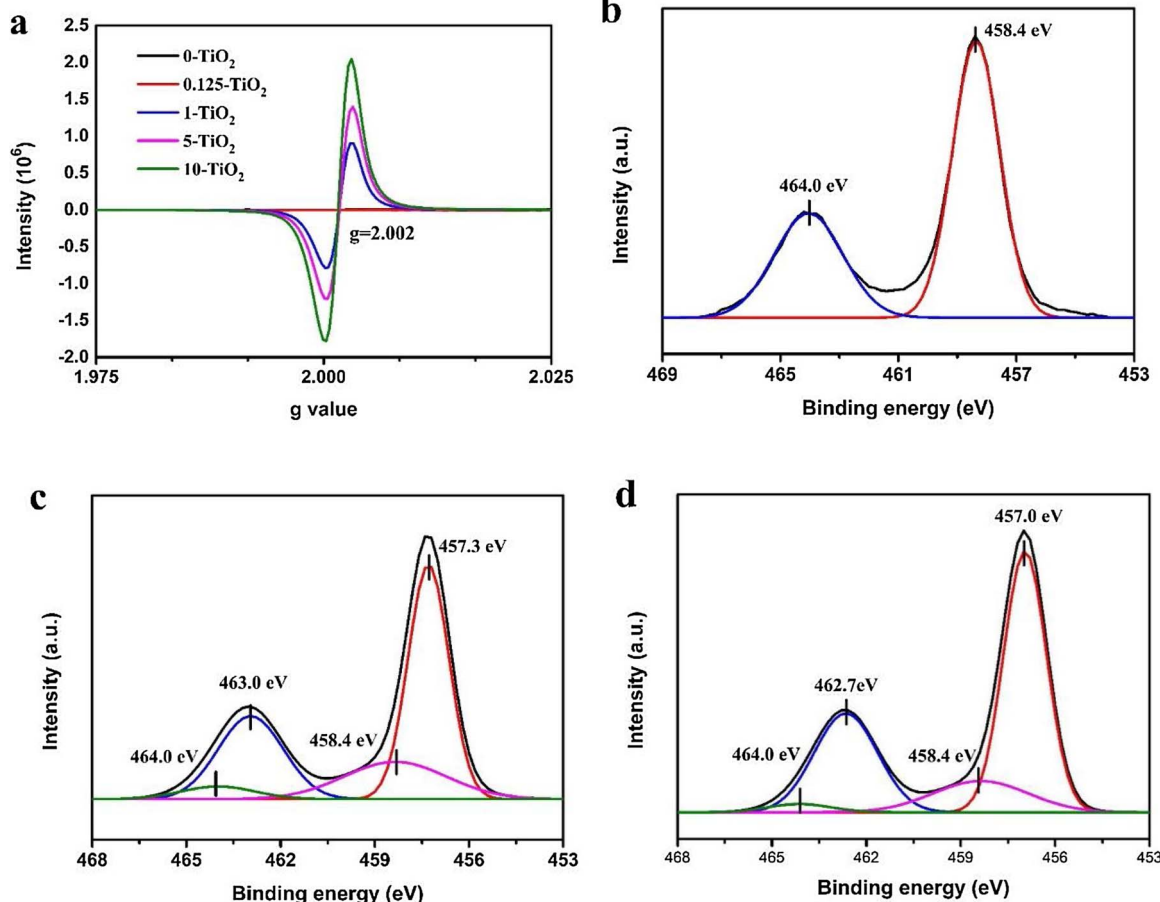


Fig. 2. (a) ESR spectra of samples prepared by using different amount Al(acac)₃ and Ti2p XPS spectra of Sample (b) 0-TiO₂ (c) 1-TiO₂ and (d) 10-TiO₂.

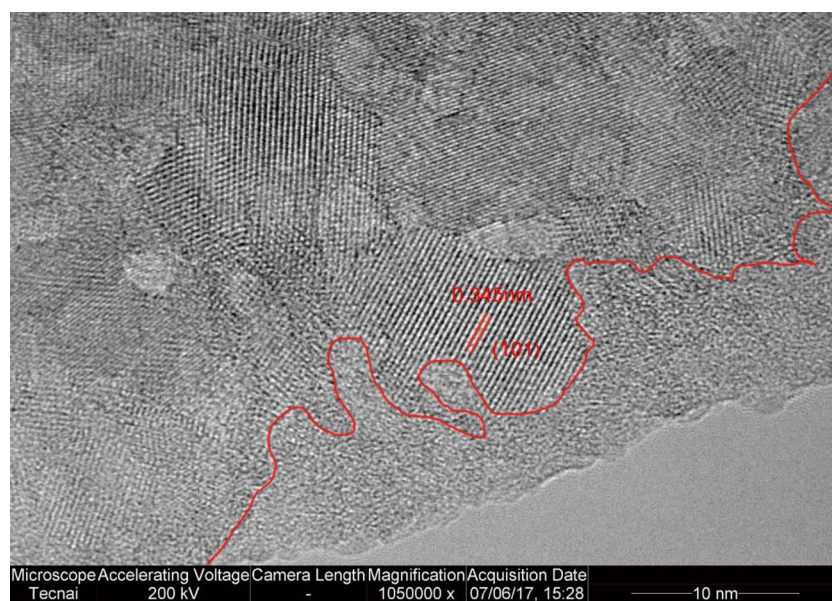


Fig. 3. HRTEM image of the as-prepared Ti^{3+} - TiO_2 . Sample 10- TiO_2 is taken as an example.

rather than anatase TiO_2 because the signal of Ti^{3+} is stronger than that of Ti^{4+} in the $\text{Ti}2\text{p}$ XPS spectra [26]. If Ti^{3+} concentrates in the bulk of samples, little signal of Ti^{3+} would be detected in the $\text{Ti}2\text{p}$ XPS spectra. Unless Ti^{3+} concentrates in the surface layer of powders (Fig. 9), the XRD patterns and XPS spectra will correspond to each other [15]. In addition, the g-value of 2.002 rather than 1.995–1.997 in the ESR spectra also supports this assumption [7,27,28]. It is considered that Ti^{3+} in the surface layer could enhance both light absorbance and charge separation while Ti^{3+} in the bulk could only improve light absorbance [29,30]. The reason why Ti^{3+} concentrates in the surface layer rather than distributes uniformly might be attributed to segregation due to the especially high solubility of $\text{Al}(\text{acac})_3$ in ethanol.

The assumption that the samples are homojunctions between Ti^{3+} - TiO_2 in the surface layer and TiO_2 in the bulk is further confirmed by HRTEM image of as-prepared Ti^{3+} - TiO_2 . As shown in Fig. 3, the surface of Ti^{3+} - TiO_2 particles is disordered and its thickness varies from 2 nm to 10 nm, indicating that the lattice of the surface layer is covered by the heavily doped Ti^{3+} - TiO_2 [31,32]. While the bulk of samples displays lattice features, with lattice spacing of 0.345 nm which is ascribed to the (101) plane of anatase TiO_2 . Almost no disordered grain can be found in the bulk, confirming that little Ti^{3+} species is distributed in the bulk. The uneven distribution of Ti^{3+} makes the homojunction between Ti^{3+} - TiO_2 in the surface layer and TiO_2 in the bulk.

O1s and C1s XPS spectra of samples are depicted in Fig. S3. As shown in Fig. S3, the peaks of 531.1 eV and 529.7 eV are ascribed to $-\text{OH}$ absorbed on the surface and Ti^{4+} - O bond of TiO_2 [33]. While a new and large peak is generated at 528.6 eV, as shown in Fig. S3b–c, which can be attributed to an ionic Ti – O bonding for Ti^{3+} - TiO_2 [34,35]. It is well known that the density of electron cloud of Ti^{3+} - O is denser than that of Ti^{4+} - O , decreasing the electron binding energy of both $\text{Ti}2\text{p}$ and O1s and resulting a high extent of ionicity of Ti – O bonding [36]. Fig. S3d shows the C1s XPS spectra for the resultant sample. The peak of 284.6 eV is the absorbed C for calibration and 288.4 eV is carbonaceous impurities on the surface [37,38].

The peak areas of the $\text{Ti}2\text{p}_{3/2}$ and O1s states are listed in Table 1. It can be observed that the peak area of absorbed $-\text{OH}$ on the surface decreases greatly for Ti^{3+} - TiO_2 in contrast to undoped TiO_2 . At the same time, the area ratio of both Ti^{3+} to Ti^{4+} and ionic oxygen to covalent oxygen increases, implying that the content of Ti^{3+} increases with the increasing amount of $\text{Al}(\text{acac})_3$ in the precursors, which corresponds to the information from ESR (Fig. 2a). Furthermore, a constant value could be got from Eq. (1),

Table 1
Peak areas of the $\text{Ti}2\text{p}_{3/2}$ and O1s states in XPS spectra.

Sample	Peak Area				
	458.4 eV	457.3 eV	531.1 eV	529.6 eV	528.7 eV
0- TiO_2	79605		211876	104796	0
1- TiO_2	49518	167898	59458	104424	172089
10- TiO_2	20939	84644	65304	81573	155133

$$\frac{S_{\text{Ti}^{3+}}/S_{\text{Ti}^{4+}}}{S_{\text{ionicO}}/S_{\text{covalentO}}} \approx 2.1 \quad (1)$$

The value is about 2.1, which confirms the theoretical simulation that one oxygen vacancy occurs with two trivalent ions [39].

The microstructure of the as-prepared Ti^{3+} - TiO_2 is characterized by N_2 adsorption-desorption isotherms and EDS elemental mapping. N_2 adsorption-desorption isotherms is employed to characterize the porous structure and specific area of samples. As shown in Fig. S4a, all samples exhibits a type IV nitrogen isotherm with a $\text{H}2$ hysteresis loop, which is ascribed to mesoporous characteristics [40–43]. The pore-size distribution obtained by BJH method from the desorption branch of the isotherm, as shown in Fig. S4b, is in a narrow range of 3–5 nm, which is useful in the photoelectrochemical and photocatalytic process. The specific area obtained by BET method, as illustrated in Table S1, decreases with the introduction of $\text{Al}(\text{acac})_3$ in the precursor. It is negative for improving the photoelectrochemical and photocatalytic activity. EDS elemental mapping is implemented to analyze the element distribution of the as-prepared samples. As shown in Fig. S5a, the as-prepared samples are composed of nanoparticles of 10 nm. The mesoporous of the samples detected by N_2 adsorption-desorption isotherms might origins from the gaps between these nanoparticles. Fig. S5b–f illustrates that the samples are composed of Ti, O and trace amounts of C with uniform distribution.

Fig. 4 displays the UV-vis diffuse reflectance spectra of the samples. It is clear that the light absorbance of Ti^{3+} - TiO_2 in the visible light region is greatly improved, implying a narrower band gap than that of undoped TiO_2 . The band gaps of the as-prepared Ti^{3+} - TiO_2 samples, as shown in Fig. S6, are got through transformed Kubelka-Munk function against photon energy [5,40]. It is found that the band gap of the obtained Ti^{3+} - TiO_2 decreases linearly from 3.11 eV to 2.78 eV with the increasing amount of Ti^{3+} . Meanwhile, a photograph of two samples is also inserted into Fig. 4. It is clearly that Ti^{3+} - TiO_2 is dark gray while

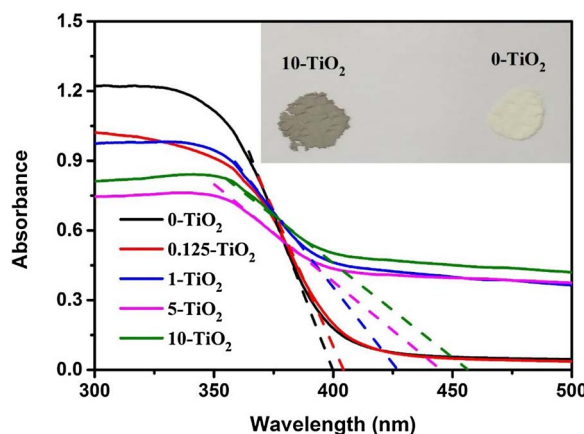


Fig. 4. UV-vis diffuse reflectance spectra of the samples. The insert is the photograph of Sample 0-TiO₂ and 10-TiO₂.

undoped TiO₂ is white in color. The light absorption could be improved for the resulted sample which is ascribed to the results of UV-vis DRS spectra [23]. The improved absorption of photocatalyst results in enhanced charge generation, which will benefit to a higher photocatalytic activity.

3.2. The synthesis mechanism of Ti³⁺-TiO₂

In order to investigate the formation mechanism of Ti³⁺ in the samples, FT-IR spectra were firstly recorded for the sols and gels of two kind samples. As shown in Fig. 5, almost no changes can be found between the sol and gel of each sample, suggesting that little chemical reaction happens from sols to gels. Table 2 summarizes the bond types derived from the FT-IR peaks according to Fig. 5 and the standard bond types of Al(acac)₃ and Hacac from infrared spectrum database from NIST (National Institute of Standards and Technology) Chemistry WebBook, SRD 69. As shown in Table 2, the peaks of the sol/gel of samples are similar to that of Al(acac)₃, but they are quite inconsistent with that of Hacac. Considering that Ti is the only introduced metal element during the synthesis of undoped TiO₂ (Sample 0-TiO₂), the spectra of the sol/gel of Sample 0-TiO₂ are inferred as the chelation of TBOT and the acetylacetone ligands as illustrated in Fig. 7a [44]. As for the sol/gel of Sample 10-TiO₂ with 10% Al(acac)₃, two pairs of peaks for the bending vibration of C–H is observed. One pair appear at 1460 cm⁻¹ and 1386 cm⁻¹, which is the same as the standard peaks of Al(acac)₃. It is ascribed to the Al(acac)₃ which is introduced in the precursor. The other pair appear at 1414 cm⁻¹ and 1361 cm⁻¹, there is a moderate shift from that of the sol/gel of Sample 0-TiO₂. Some chemical changes are assumed to occur for the chelation structure of TBOT

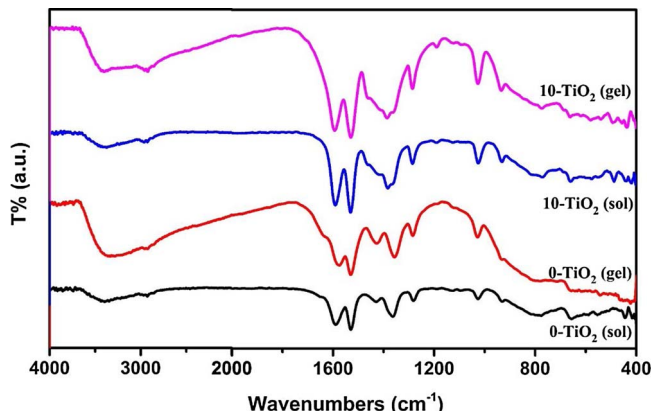


Fig. 5. FT-IR spectra of the sols and gels of samples.

Table 2
Bond types of FT-IR spectra of samples and Al(acac)₃.

Bond Type	Wavenumbers (cm ⁻¹)			
	0-TiO ₂	10-TiO ₂	Al(acac) ₃	Hacac
ν OH	3333	3404	2924	3006/2964/2924
ν C–H	2926	2923	2924	3006/2964/2924
ν C=O	1574	1593	1593	1729/1710
	1530	1529	1534	1616
δ C–H	1426	1460/1414	1466	1420
	1357	1386/1361	1387	1360
ν C–O	1285	1285	1290	1249
	1028	1027	1028	1156

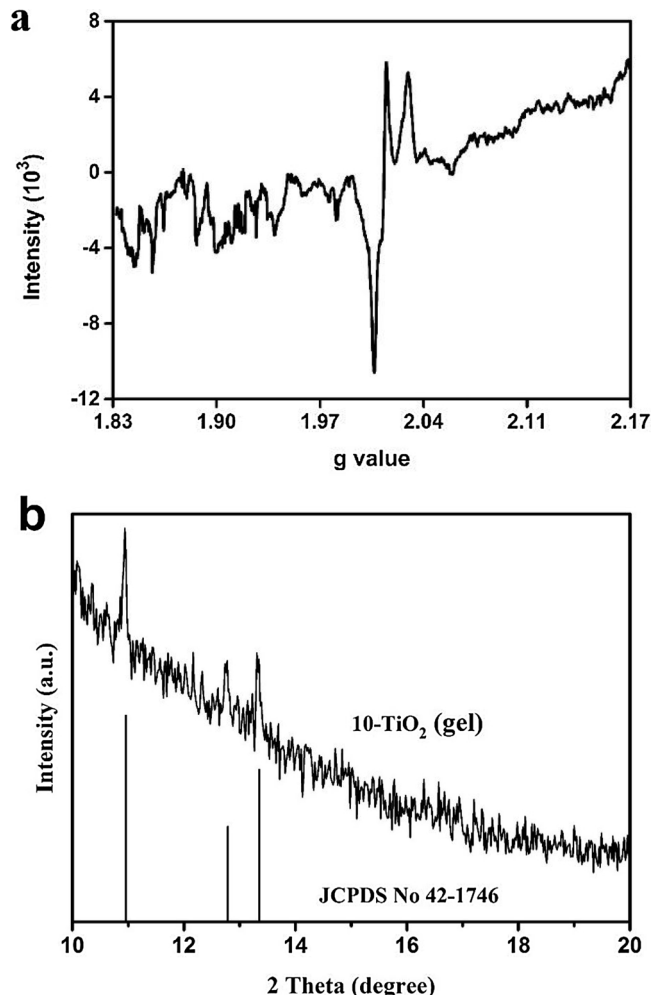
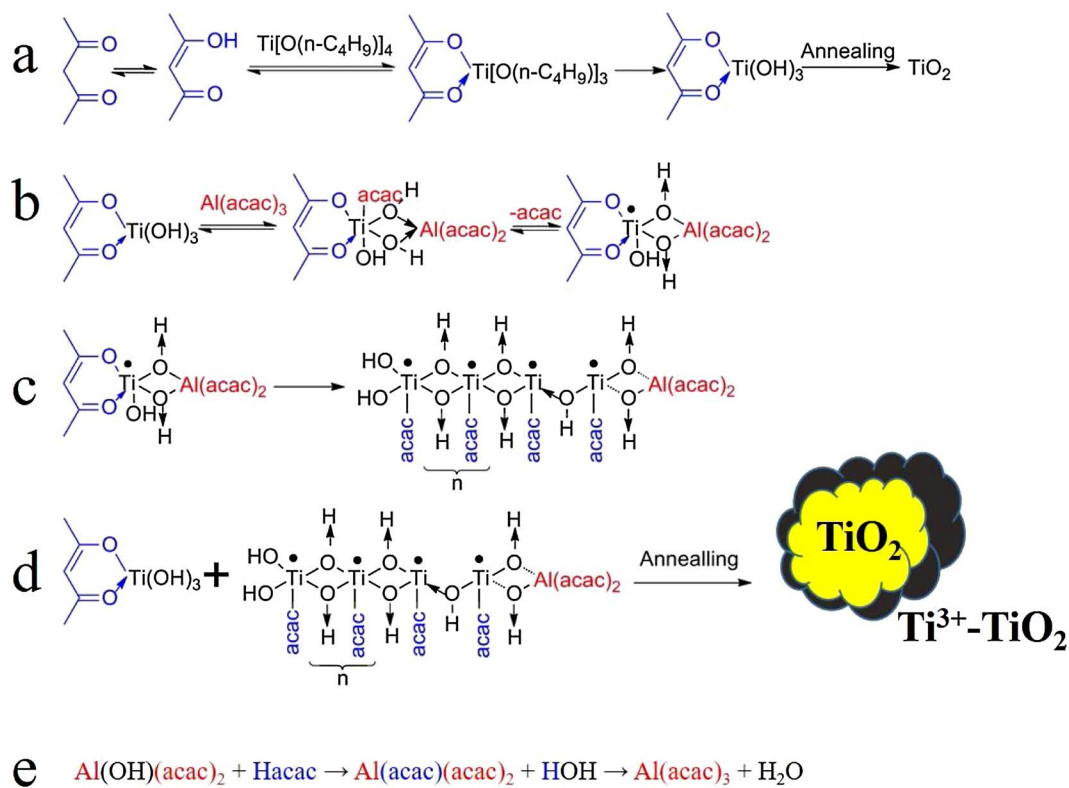


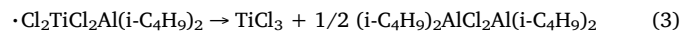
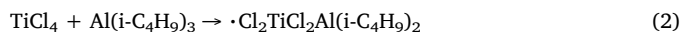
Fig. 6. (a) ESR spectrum and (b) XRD pattern of the gel of as-prepared Ti³⁺-TiO₂. Sample 10-TiO₂ is taken as an example.

and acetylacetone.

Fig. 6a shows the ESR spectrum for the gel of Sample 10-TiO₂. It can be seen that the intensity is three orders of magnitude less than that of the annealed one, as compared to Fig. 2a. Furthermore, both the position and shape of the signal are different. It can be concluded that no Ti³⁺ was formed from the sol to gel. Fig. 6b shows XRD pattern of the gel of Sample 10-TiO₂. It matches well with Al(acac)₃ (JCPDS no. 42-1746), reflecting the presence of Al(acac)₃ in the gel. While the peaks of Al(acac)₃ disappear after annealing, as illustrated in the XRD patterns in Fig. 1a, indicating that the Al(acac)₃ is removed during the annealing process. In view of the weak ESR signal, there should be some substance with unpaired electron in the sols/gels.

Fig. 7. The growing mechanism of the gel of (a) TiO_2 , (b-d) $\text{Ti}^{3+}\text{-TiO}_2$ and (e) $\text{Al}(\text{acac})_3$.

On the foundation of the proof of Ti^{3+} and FT-IR results, the growing mechanism of Ti^{3+} in our sample is proposed with reference to the research of Ziegler-Natta catalysts due to their similar precursor and products composed of Ti^{3+} . Tkáč [33–35] studied the reduction mechanism of Ziegler-Natta catalysts by ESR and FT-IR systematically and discovered the bimetallic complexes alkylated intermediate. The reactions were proposed as the follows (Eqs. (2) and (3) [45]):



Besides the steric hindrance of $-\text{OH}$ and $-\text{acac}$, $-\text{OH}$ from hydrolyzing intermediate of TBOT is nucleophilic as Cl^- from TiCl_4 while $-\text{acac}$ from $\text{Al}(\text{acac})_3$ is electrophilic as $(\text{i-C}_4\text{H}_9)_3$ from $\text{Al}(\text{i-C}_4\text{H}_9)_3$ because of its conjugated π bonds, making the system of TBOT and $\text{Al}(\text{acac})_3$ a Ziegler-Natta composition. According to the mechanism of Ziegler-Natta catalysts, the scheme is conjectured as shown in Fig. 7a–e. On account of the fact that Al^{3+} is lewis acid as well as the semi-diameter of Al^{3+} (0.050 nm) is smaller in contrast to Ti^{4+} (0.061 nm). The interaction of $\text{Al}(\text{acac})_3$ and $\text{Ti}(\text{acac})(\text{OH})_3$ gives rise to the exchange of $-\text{OH}$ and $-\text{acac}$ by coordination bond, which starts the formation of Ti^{3+} . The unstable intermediate product, $\text{Ti}(\text{acac})_2(\text{OH})_3\text{Al}(\text{acac})_2$, may quickly decomposes into the radical as $\cdot\text{Ti}(\text{acac})(\text{OH})_3\text{Al}(\text{acac})_2$ and a $\text{Ti}^{4+} \rightarrow \text{Ti}^{3+}$ reduction happens accordingly. Under the driving force of the crystal field effect, which transforms hexahedral structure into octahedral structure, the bimetallic Ti-Al radicals grow to crystalline as shown in Fig. 7c [46]. It may be the Ti-Al bimetallic crystalline and the leaving group of $\text{Al}(\text{acac})_3$ that generate the FT-IR signals of the sol/gel of samples with $\text{Al}(\text{acac})_3$. The paramagnetism is so little for the gel because the mutual compensation of the free electrons of Ti^{3+} with opposed spins [47]. During the annealing process, the organic aluminium evaporates and the crystalline decomposes into $\text{Ti}^{3+}\text{-TiO}_2$, as shown in Fig. 7d. It should be acknowledged that experimental evidences are necessary to confirm this mechanism.

On account of the fact that the $\text{Al}(\text{acac})_3$ which participates in the reaction would return back to $\text{Al}(\text{acac})_3$, as indicated in XRD (Fig. 6b) and FT-IR (Table 2) results of the gels of samples. The destination of $\text{Al}(\text{acac})_3$ is proposed as shown in Fig. 7e. Every leaving group of $\text{Al}(\text{acac})_2(\text{OH})$ would be restored to $\text{Al}(\text{acac})_3$ owing to the existence of Hacac, making $\text{Al}(\text{acac})_3$ acting as the catalyst in the following redox reaction: $\text{Ti}^{4+} + \text{Hacac} \rightarrow \text{Ti}^{3+} + \cdot\text{acac}$. The thermodynamic feasibility of this reaction has been proved by Aronne et al. [25]. However, this reaction may be hard to happen in kinetics. On one hand, Sample 0- TiO_2 is produced by TBOT and Hacac, little Ti^{3+} is detected by ESR. On the other hand, Hacac has been used as the anti-hydrolysis agent in undoped TiO_2 preparation via sol-gel method for tens of years. It is $\text{Al}(\text{acac})_3$ that catalyzes this reaction and produced heavily doped $\text{Ti}^{3+}\text{-TiO}_2$ samples.

3.3. Photoelectrochemical and photocatalytic activities of samples

Electrochemical impedance spectroscopy (EIS) is employed to analyze the charge transfer process and interface reaction. Fig. 8a shows the Nyquist plots of as-prepared electrodes under simulated solar irradiation. The plots consist of semicircles at high frequencies and straight lines at low frequencies. It can be seen that the arc semidiameters become smaller greatly for the samples with Ti^{3+} , illustrating that the electron transfer resistances decrease with the doping of Ti^{3+} in TiO_2 . The equivalent circuit model [48,49] is inserted in Fig. 8a and their impedance elements are analyzed by Z-View. All simulated results are listed in Table 3, where R_i is internal resistance, CPE is constant phase element, R_{ct} is the charge transfer at the working electrode/electrolyte interface and W_s is the Warburg diffusion process in the electrolyte [50]. In view of the fact that the charge transfer at the working electrode/electrolyte interface is limited by the slowest step of the charge transfer, the charge transfer resistance is usually used to characterize the rates of charge transport of carriers in semiconductors [51]. The occurrence of Warburg diffusion process illustrates the changes of species in the electrolyte, which is caused by chemical reactions [52].

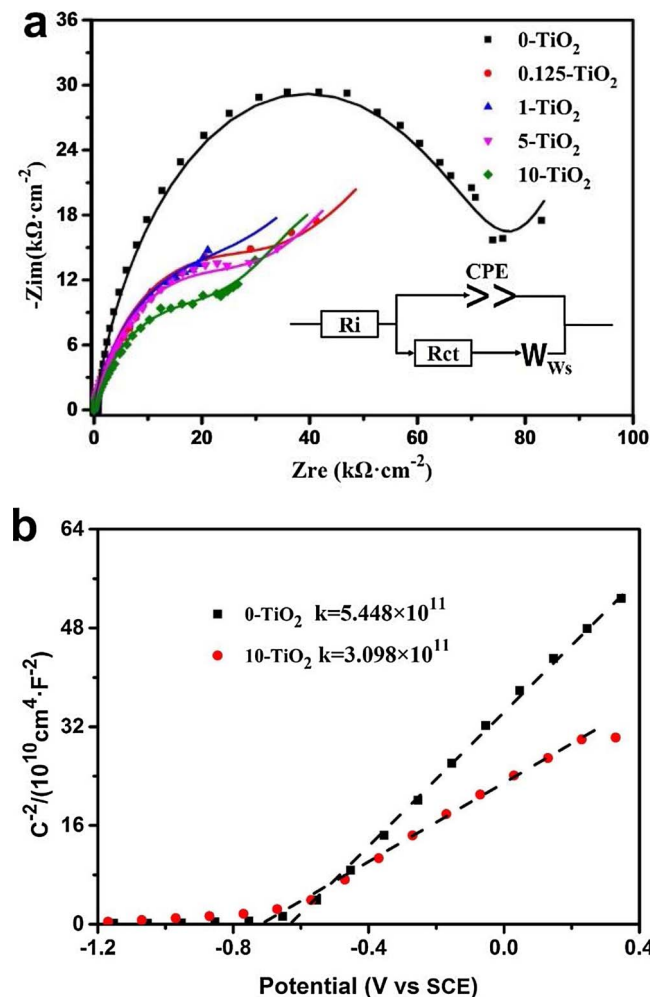


Fig. 8. (a) Nyquist plots and the fitting line of as-prepared electrodes under simulated solar irradiation (the insert is the equivalent circuit model) and (b) Mott-Schottky plots of as-prepared electrodes under dark in 0.5 M Na₂SO₄ solution (vs. SCE).

Thus, the Warburg impedance could be used to evaluate the rates of interface reaction indirectly because the concentration diffusion of species can not be faster than interface reaction if an electrochemical process is controlled by diffusion.

Fig. S7 shows the Nyquist plots of as-prepared electrodes under dark and its equivalent circuit model. Owing to the lack of excitation carriers, the charge transfer resistances are the charge transfers between space charge layer and electrolyte. They are so large in contrast to those under simulated solar irradiation that the electric double layers are nearly pure capacitances. Although the impedance under dark is sometimes applied to reflect the original property of materials [53], it

Table 3
The fitted impedance dates based on equivalent circuit.

Electrodes	R _i (Ω·cm ²)	CPE-T	CPE-P	W _s (Ω·cm ²)	R _{ct} (Ω·cm ²)
0-TiO ₂	36.1	9.4 × 10 ⁻⁶	0.82	1.41 × 10 ⁵	7.5 × 10 ⁴
0.125-TiO ₂	32.7	1.5 × 10 ⁻⁵	0.78	1.37 × 10 ⁵	2.9 × 10 ⁴
1-TiO ₂	51.9	3.3 × 10 ⁻⁵	0.78	1.08 × 10 ⁵	2.6 × 10 ⁴
5-TiO ₂	49.6	1.3 × 10 ⁻⁵	0.78	8.2 × 10 ⁴	2.6 × 10 ⁴
10-TiO ₂	52.0	2.5 × 10 ⁻⁵	0.82	6.3 × 10 ⁴	2.0 × 10 ⁴

could not describe the character during photocatalysis [54,55] because of the lack of photo-induced carrier.

From the data in Table 3, it is confirmed that the Warburg impedance calculated from the straight line at low frequency decreases with the higher ratio of Ti³⁺ in TiO₂ and it should be reasonable since Ti³⁺ could act as the active sites [56] in chemical process. The decrease of the Warburg impedance accelerates the rate of interface reactions. As shown in Table 3, the charge transfer resistance (R_{ct}) also decreases with the increasing density of Ti³⁺ in TiO₂, which benefits the transport of carriers. It is due to the enhanced conductivity of samples deriving from the unpaired electrons introduced by Ti³⁺. The conductivity of n-type semiconductor judged by the number of electrons is the key factor to charge transport. The increased density of electrons by the presence of Ti³⁺ leads to higher conductivity which is helpful for the transport of electrons and holes.

The density of electrons, as the majority carriers in n-type TiO₂, is calculated by means of the differential form of Mott-Schottky formula (Eq. (4)),

$$N_d = \frac{2}{\varepsilon \varepsilon_0 e} \frac{d(E - E_{fb} - \frac{kT}{e})}{d(1/C^2)} \quad (4)$$

where N_d is charge carrier densities, ε₀ is vacuum permittivity (8.854 × 10⁻¹⁴ F/cm), ε is permittivity of anatase TiO₂, e equals 1.6 × 10⁻¹⁹ C and d(E-E_{fb}-kT/e)/d(1/C²) is the reciprocal of the slope of Mott-Schottky curve [57]. As calculated by Eq. (4), the density of electrons increases to 5.713 × 10¹⁸ cm⁻³ of Sample 10-TiO₂ (Ti³⁺ self-doped TiO₂) from 3.239 × 10¹⁸ cm⁻³ of Sample 0-TiO₂ (undoped TiO₂).

The value of flat band potential, E_{fb}, is calculated by the horizontal intercept of the tangent line of Mott-Schottky plots [58,59]. From Fig. 8b, the flat band potential is -0.71 V (vs. SCE) for Sample 10-TiO₂, while it is -0.63 V (vs. SCE) for undoped TiO₂ (Sample 0-TiO₂), which means the conduction band becomes more negative owing to the presence Ti³⁺ for the resultant samples. For n-type semiconductors, the flat band potentials are approximately equal to the bottom of their conduction bands [60]. Now that the surface space charge layer plays a dominant role in the capacitance-voltage characteristics of Mott-Schottky plots [51]. Thus, the calculated flat band potentials can reflect the location of the conduction bands of samples in the surface layer (< 50 nm [61]). The energy band of a semiconductor could be confirmed by the combination of flat band potential from Mott-Schottky

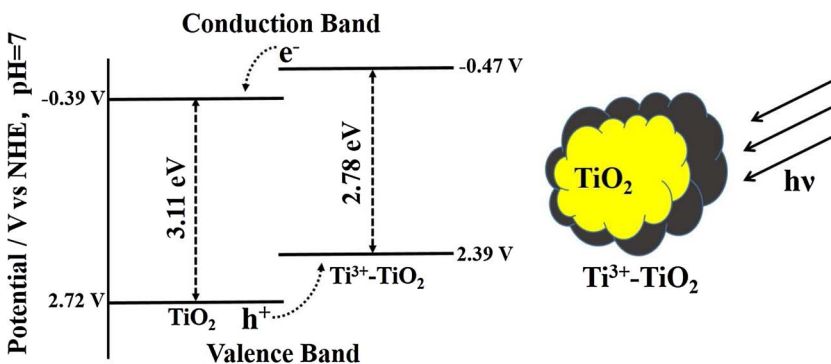


Fig. 9. Schematic of the energy band of as-prepared Ti³⁺-TiO₂ with charge migration and separation. Sample 10-TiO₂ is taken as an example and the potential has been converted from vs. SCE into vs. NHE.

curve and band gap from UV-vis DRS spectra. For the as-prepared samples, the energy band of Ti^{3+} - TiO_2 in the surface layer is got from those of Sample 10- TiO_2 while the undoped TiO_2 in the bulk is got from those of Sample 0- TiO_2 . Accordingly, the schematic of the energy band of as-prepared Ti^{3+} - TiO_2 is obtained as displayed in Fig. 9. VB XPS spectra is employed to confirm the position of valence band. As shown in Fig. S8, the valence band of Sample 10- TiO_2 is -0.50 eV lower than that of Sample 0- TiO_2 , which is consistent with the result of the assumption from Mott–Schottky curve and UV-vis DRS spectra. The energy band of the as-prepared Ti^{3+} - TiO_2 is formed as a type-II staggered gap, which is to the benefit of charge migration and separation. The Ti^{3+} in the surface layer promotes the light absorption and the homojunction helps speeding up the separation of charge carriers.

During the photoelectrochemical reaction, both interface reactions from electrode to electrolyte and charge transfers in semiconductors are indispensable. The photocatalytic activities of photocatalysts are controlled by both of them. Now that the calculated value of Warburg impedance is larger than that of electron transfer resistance for every sample, it is assumed that the interface reactions are slower than charge transport of carriers in semiconductors, which is ascribed to the previous study [62]. The acceleration of charge transport and interface reactions could improve the photocatalytic activities.

The photoelectrochemical activity is measured by transient photocurrent curves of electrodes at 0 V (vs. SCE). A Xenon lamp is carried as the simulated solar irradiation. As illustrated in Fig. 10a, when the light is turned on, the current jumps to a high peak and then drops to a stable level. It is the active substances absorbed on the surface that cause the

high peak [63]. The photocurrent on/off transients of samples increase linearly for the samples with Ti^{3+} , indicating enhanced the photoelectrochemical activity with the introduction of Ti^{3+} . For wide-band-gap semiconducting electrodes, the intensity of photocurrent is judged by Eq. (5) [64].

$$J^2 = (q\varphi_0\alpha W_0)^2 (V - V_{fb}) \quad (5)$$

J is the current density, q is the charge transferred per ion, φ_0 is the photon flux, α is the optical absorption, V is the applied potential, V_{fb} is the flat-band potential and W_0 is the depletion-layer width when $V - V_{fb} = 1$. The enhanced photoelectrochemical activities of Ti^{3+} - TiO_2 are the resultant force of higher absorption coefficient (α) and quicker charge transport (W_0).

The photodegradation of MB is implemented in order to measure its photocatalytic activity. As shown in Fig. 10b, the speed of photodegradation activity is calculated according to $\ln(C_0/C) = kt$ since the photodegradation of MB is a pseudo-first-order reaction in kinetic. C_0 is the equilibrium concentration before irradiation and C is the instantaneous concentration during the photocatalytic process. The photodegradation efficiency of TiO_2 is enhanced after doping of Ti^{3+} and Sample 1- TiO_2 and 5- TiO_2 show the best photocatalytic activity.

The photocatalytic activity of samples does not improve linearly with the increasing density of Ti^{3+} as the photoelectrochemical activity. The reasons might be particle size, crystallinity, surface area and morphology. The as-prepared samples show similar characteristics in particle size, crystallinity and porous structure as shown in Fig. 1, Fig. S2, Fig. S5, and Fig. S4b. Although the specific area of samples are different, it decreases with improvement of photocatalytic activities. The disadvantage of specific area is completely made up by the improvement of charge generation, charge transport and interface reactions caused by Ti^{3+} and homojunction, illustrating that the specific area is not the dominant factor for the photocatalytic activities of the as-prepared Ti^{3+} - TiO_2 . All of the possibility above have been excluded. The difference of reaction sites between photocatalytic and photoelectrochemical process might be answer to this question [65,66]. For photoelectrochemical process, the oxidation reaction and reduction reaction happen on working electrode and counter electrode respectively. The Ti^{3+} on the surface would not act as the recombination center. For photocatalytic process, the oxidation reaction and reduction reaction happen on the same sites. The surface recombination of photo-induced carriers besides Ti^{3+} could not be ignored.

4. Conclusions

In this work, we have shown that $\text{Al}(\text{acac})_3$ can be used as the catalyst to synthesize Ti^{3+} - TiO_2 by sol-gel method in air. Ti^{3+} is heavily doped into TiO_2 and there is a homojunction in the samples between Ti^{3+} heavily doped TiO_2 in the surface layer and undoped TiO_2 in the bulk. Through the study on the sols and gels of samples and the reference of the mechanism of Ziegler-Natta catalysts, the forming mechanism of Ti^{3+} is proposed as the combination of steric hindrance effect, Lewis acid-base reaction and crystal field effect. $\text{Al}(\text{acac})_3$ acts as the catalyst in this reaction because every $\text{Al}(\text{acac})_3$ which participates in the reaction would return back to $\text{Al}(\text{acac})_3$. UV-vis DRS shows improved light response for resultant samples. Electrochemical impedance spectroscopy measurements indicate that both charge transport and interface reaction improved greatly. Enhanced photoelectrochemical and photocatalytic activities were also demonstrated by the transient photocurrent and photodegradation of MB under UV-vis light. In contrast with the reported methods, this work proposes a novel direction to obtain Ti^{3+} - TiO_2 through $\text{Al}(\text{acac})_3$ as catalyst and we believe this method could be extended to the preparation of MO_x (M belongs to IIIB to VIIB elements) with surface oxygen vacancy.

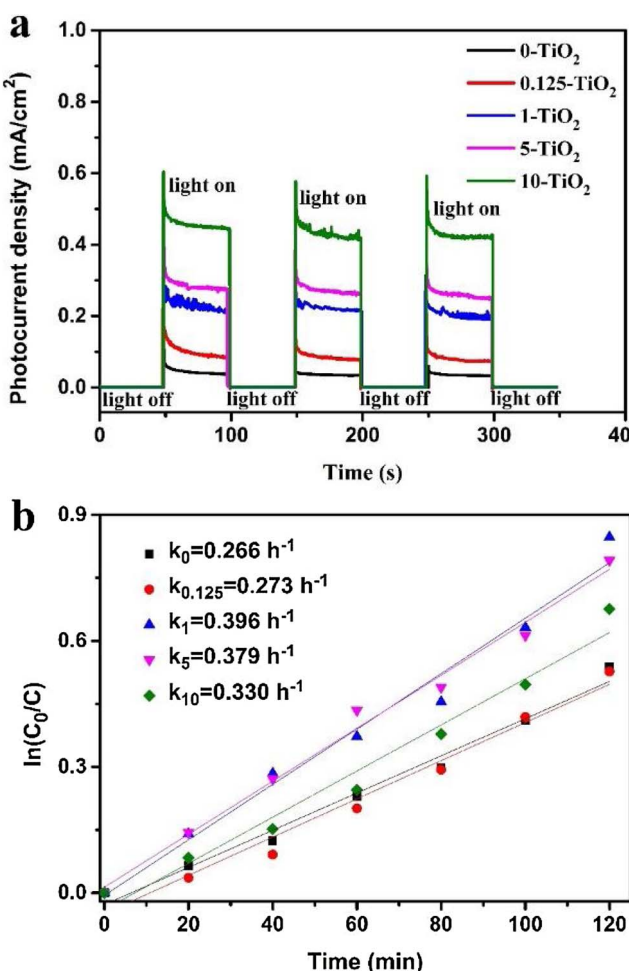


Fig. 10. (a) Transient photocurrent curves of as-prepared electrodes with 0.5 M Na_2SO_4 solution under UV-vis light irradiation at 0 V (vs. SCE). (b) Photocatalytic activity of samples with different amount Ti^{3+} in degradation of MB under UV-vis light.

Acknowledgments

This work has been supported by the Natural Science Foundation of China (No. 21273047) and Key Laboratory of Functional Inorganic Material Chemistry (Heilongjiang University), Ministry of Education. The authors appreciate all referees for valuable comments as well. We really appreciate the referee's valuable comments, which have greatly improved the quality of the manuscript.

Appendix A. Supplementary data

Supplementary data associated with this article can be found, in the online version, at <http://dx.doi.org/10.1016/j.apcatb.2017.10.057>.

References

- [1] Y. Ma, X.L. Wang, Y.S. Jia, X.B. Chen, H.X. Han, C. Li, Titanium dioxide-based nanomaterials for photocatalytic fuel generations, *Chem. Rev.* 114 (2014) 9987–10043.
- [2] M. Grätzel, Photoelectrochemical cells, *Nature* 414 (2001) 338–344.
- [3] X.B. Chen, L. Liu, P.Y. Yu, S.S. Mao, Increasing solar absorption for photocatalysis with black hydrogenated titanium dioxide nanocrystals, *Science* 331 (2011) 746–750.
- [4] Y. Zhang, Z. Xing, X. Liu, Z.Z. Li, X.Y. Wu, J.J. Jiang, M. Li, Q. Zhu, W. Zhou, Ti^{3+} self-doped blue TiO_2 (B) single-crystalline nanorods for efficient solar-driven photocatalytic performance, *ACS Appl. Mater. Interface* 8 (2016) 26851–26859.
- [5] W.Z. Fang, M.Y. Xing, J.L. Zhang, A new approach to prepare Ti^{3+} self-doped TiO_2 via $NaBH_4$ reduction and hydrochloric acid treatment, *Appl. Catal. B-Environ.* 160–161 (2014) 240–246.
- [6] Z.K. Zheng, B.B. Huang, X.D. Meng, J.P. Wang, S.Y. Wang, Z.Z. Lou, Z.Y. Wang, X.Y. Qin, X.Y. Zhang, Y. Dai, Metallic zinc- assisted synthesis of Ti^{3+} self-doped TiO_2 with tunable phase composition and visible-light photocatalytic activity, *Chem. Commun.* 49 (2013) 868–870.
- [7] F.F. Wang, W.N. Ge, T. Shen, B.J. Ye, Z.P. Fu, Y.L. Lu, The effect of bulk/surface defects ratio change on the photocatalysis of TiO_2 nanosheet film, *Appl. Surf. Sci.* 410 (2017) 513–518.
- [8] B.J. Jiang, Y.Q. Tang, Y. Qu, J.Q. Wang, Y. Xie, C.G. Tian, W. Zhou, H.G. Fu, Thin carbon layer coated Ti^{3+} - TiO_2 nanocrystallites for visible-light driven photocatalysis, *Nanoscale* 7 (2015) 5035–5045.
- [9] W.H. Saputera, G. Mul, M.S. Hamdy, Ti^{3+} -containing titania: synthesis tactics and photocatalytic performance, *Catal. Today* 246 (2015) 60–66.
- [10] H. Yin, T.Q. Lin, C.Y. Yang, Z. Wang, G.L. Zhu, T. Xu, X.M. Xie, F.Q. Huang, M.H. Jiang, Gray TiO_2 nanowires synthesized by aluminum-mediated reduction and their excellent photocatalytic activity for water cleaning, *Chem. A-Eur. J.* 19 (2013) 13313–13316.
- [11] Y. Zhou, C.H. Chen, N.N. Wang, Y.Y. Li, H.M. Ding, Stable Ti^{3+} self-doped anatase-rutile mixed TiO_2 with enhanced visible light utilization and durability, *J. Phys. Chem. C* 120 (2016) 6116–6124.
- [12] M.S. Hamdy, W.H. Saputera, E.J. Groenen, G. Mul, A novel TiO_2 composite for photocatalytic wastewater treatment, *J. Catal.* 310 (2014) 75–83.
- [13] X. Liu, H. Xu, L.R. Grabstanowicz, S.M. Gao, Z.Z. Lou, W.J. Wang, B.B. Huang, Y. Dai, T. Xu, Ti^{3+} self-doped TiO_{2-x} anatase nanoparticles via oxidation of TiH_2 in H_2O_2 , *Catal. Today* 225 (2014) 80–89.
- [14] K. Li, S.M. Gao, Q.Y. Wang, H. Xu, Z.Y. Wang, B.B. Huang, Y. Dai, J. Lu, In-situ-reduced synthesis of Ti^{3+} self-doped $TiO_2/g-C_3N_4$ heterojunctions with high photocatalytic performance under LED light irradiation, *ACS Appl. Mater. Interface* 7 (2015) 9023–9030.
- [15] K. Li, Z. Huang, X. Zeng, B.B. Huang, S.M. Gao, J. Lu, Synergetic Effect of Ti^{3+} and oxygen doping on enhancing photoelectrochemical and photocatalytic properties of $TiO_2/g-C_3N_4$ heterojunctions, *ACS Appl. Mater. Interface* 9 (2017) 11577–11586.
- [16] J.H. Cai, Z.A. Huang, K.L. Lv, J. Sun, K.J. Deng, Ti powder-assisted synthesis of Ti^{3+} self-doped TiO_2 nanosheets with enhanced visible-light photoactivity, *RSC Adv.* 4 (2014) 19588–19593.
- [17] J. Lee, X.L. Cui, Facile preparation of Ti^{3+} self-doped TiO_2 microspheres with lichi-like surface through selective etching, *Mater. Lett.* 175 (2016) 114–117.
- [18] J. Liu, R.E. Saw, Y.H. Kiang, Calculation of effective penetration depth in X-ray diffraction for pharmaceutical solids, *J. Pharm. Sci.* 99 (2010) 3807–3814.
- [19] L. Liu, X.B. Chen, Titanium dioxide nanomaterials: self-structural modifications, *Chem. Rev.* 114 (2014) 9890–9918.
- [20] Q.Q. Shang, X. Huang, X. Tan, T. Yu, High activity Ti^{3+} -modified brookite TiO_2 /graphene nanocomposites with specific facets exposed for water splitting, *Ind. Eng. Chem. Res.* 56 (2017) 9098–9106.
- [21] R.P. Netterfield, P.J. Martin, C.G. Pacey, W.G. Sainty, D.R. Mckenzie, G. Auchterlonie, Ion-assisted deposition of mixed TiO_2 - SiO_2 films, *J. Appl. Phys.* 66 (1989) 1805–1809.
- [22] P. Chen, A novel synthesis of Ti^{3+} self-doped Ag_2O/TiO_2 (p-n) nano-heterojunctions for enhanced visible photocatalytic activity, *Mater. Lett.* 163 (2016) 130–133.
- [23] D.M.D.L. Santos, J. Navas, A. Sánchez-Coronilla, R. Alcántara, C. Fernández-Lorenzo, J. Martín-Calleja, Highly Al-doped TiO_2 nanoparticles produced by ball mill method: structural and electronic characterization, *Mater. Res. Bull.* 70 (2015) 704–711.
- [24] T. Sekiya, Y. Takeda, S. Ohya, T. Kodaira, UV irradiation effect on Al-doped anatase titanium dioxide, *Phys. Status Solidi C* 8 (2011) 173–176.
- [25] S.J. Geng, S. Zhang, H. Onishi, XPS applications in thin films research, *Mater. Technol.* 17 (2002) 234–240.
- [26] X.Y. Tao, J.G. Wang, Z.G. Ying, Q.X. Cai, G.Y. Zheng, Y.P. Gan, H. Huang, Y. Xia, C. Liang, W.K. Zhang, Y. Cui, Strong sulfur binding with conducting Magnéli-phase $Ti_{n}O_{2n-1}$ nanomaterials for improving lithium-sulfur batteries, *Nano. Lett.* 14 (2014) 5288–5294.
- [27] C.D. Valentini, G. Pacchioni, Reduced and n-type doped TiO_2 : nature of Ti^{3+} species, *J. Phys. Chem. C* 113 (2009) 20543–20552.
- [28] A. Aronne, M. Fantauzzi, C. Imparato, D. Atzei, L.D. Stefano, G. D'Errico, F. Sannino, I. Rea, D. Pirozzi, B. Elsener, P. Pernice, A. Rossi, Electronic properties of TiO_2 -based materials characterized by high Ti^{3+} self-doping and low recombination rate of electron-hole pairs, *RSC Adv.* 7 (2017) 2373–2381.
- [29] Y. Wang, M. Jing, M. Zhang, J.J. Yang, Facile synthesis and photocatalytic activity of platinum decorated $TiO_{2-x}N_x$: perspective to oxygen vacancies and chemical state of dopants, *Catal. Commun.* 20 (2012) 46–50.
- [30] H.Y. Li, F.Z. Ren, J.F. Liu, Q.L. Wang, Q.Y. Li, J.J. Yang, Y.X. Wang, Endowing single-electron-trapped oxygen vacancy self-modified titanium dioxide with visible-light photocatalytic activity by grafting Fe(III) nanocluster, *Appl. Catal. B-Environ.* 172–173 (2015) 37–45.
- [31] Y.H. Lv, Y.Y. Zhu, Y.F. Zhu, Enhanced photocatalytic performance for the $BiPO_{4-x}$ nanorod induced by surface oxygen vacancy, *J. Phys. Chem. C* 117 (2013) 18520–18528.
- [32] Y.H. Lv, Y.F. Liu, Y.Y. Zhu, Y.F. Zhu, Surface oxygen vacancy induced photocatalytic performance enhancement of a $BiPO_4$ nanorod, *J. Mater. Chem. A* 2 (2014) 1174–1182.
- [33] X.Y. Zhang, Y.J. Sun, X.L. Cui, Z.Y. Jiang, Carbon-incorporated TiO_2 microspheres: facile flame assisted hydrolysis of tetrabutyl orthotitanate and photocatalytic hydrogen production, *Int. J. Hydrogen Energy* 37 (2012) 1356–1365.
- [34] A.I. Boronin, S.V. Koscheev, G.M. Zhidomirov, XPS and UPS study of oxygen states on silver, *J. Electron. Spectrosc. Related Phenom.* 96 (1998) 43–51.
- [35] S. Ladas, S. Kennou, S. Bebelis, C.G. Vayenas, Origin of non-faradaic electrochemical modification of catalytic activity, *J. Phys. Chem.* 97 (1993) 8845–8848.
- [36] S.G. Neophytides, S. Zafeiratos, S. Kennou, XPS characterization of the electrochemically generated O species on a Au electrode evaporated on Y_2O_3 -stabilized ZrO_2 (100), *Solid State Ion.* 136–137 (2000) 801–806.
- [37] U. Gelius, P.F. Heden, J. Hedman, B.J. Lindberg, R. Manne, R. Nordberg, C. Nordling, K. Siegbahn, Molecular spectroscopy by means of ESCA III, *Carbon Compounds*, *Phys. Scr.* 2 (1970) 70–80.
- [38] H. Irie, Y. Watanabe, K. Hashimoto, Carbon-doped anatase TiO_2 powders as a visible-light sensitive photocatalyst, *Chem. Lett.* 32 (2003) 772–773.
- [39] C. Gionco, S. Livraghi, S. Maurelli, E. Giannello, S. Tosoni, C.D. Valentini, G. Pacchioni, Al- and Ga-doped TiO_2 , ZrO_2 , and HfO_2 : the nature of O 2p trapped holes from a combined electron paramagnetic resonance (EPR) and density functional theory (DFT) study, *Chem. Mater.* 27 (2015) 3936–3945.
- [40] Y. Chen, W.Z. Li, J.Y. Wang, Y.L. Gan, L. Liu, M.T. Ju, Microwave-assisted ionic liquid synthesis of Ti^{3+} self-doped TiO_2 hollow nanocrystals with enhanced visible-light photoactivity, *Appl. Catal. B: Environ.* 191 (2016) 94–105.
- [41] J.X. Low, I. Cheng, J.G. Yu, Surface modification and enhanced photocatalytic CO_2 reduction performance of TiO_2 : a review, *Appl. Surf. Sci.* 392 (2017) 658–686.
- [42] Y.Q. Zhu, M.W. Shah, C.Y. Wang, Insight into the role of Ti^{3+} in photocatalytic performance of shuriken-shaped $BiVO_4/TiO_{2-x}$ heterojunction, *Appl. Catal. B: Environ.* 203 (2017) 526–532.
- [43] M.C. Wen, S.S. Zhang, W.R. Dai, G.S. Li, D.Q. Zhang, In situ synthesis of Ti^{3+} self-doped mesoporous TiO_2 as a durable photocatalyst for environmental remediation, *Chin. J. Catal.* 36 (2015) 2095–2102.
- [44] D. Hoebbel, T. Reinert, H. Schmidt, E. Arpac, On the hydrolytic stability of organic ligands in Al-: Ti- and Zr-alkoxide complexes, *J. Sol-Gel Sci. Technol.* 10 (1997) 115–126.
- [45] A. Tkáč, On the theory of activity of Ziegler-Natta catalysts $[TiCl_4 + Al(i-C_4H_9)_3]$. II. Mechanism of the $Ti^{4+} \rightarrow Ti^{3+}$ reduction and of the formation of bimetallic complexes studied by infrared spectra analysis, *Collect. Czech. Chem. Commun.* 33 (1968) 2004–2018.
- [46] A. Tkáč, On the theory of activity of Ziegler-Natta catalysts $[TiCl_4 + Al(i-C_4H_9)_3]$. III. Structure of active centres during heterogeneous polymerization of isoprene, *Collect. Czech. Chem. Commun.* 33 (1968) 3001–3025.
- [47] A. Tkáč, On the theory of activity of Ziegler-Natta catalysts $[TiCl_4 + Al(i-C_4H_9)_3]$. I. EPR spectra and structure of Ti-Al complexes, *Collect. Czech. Chem. Commun.* 33 (1968) 1629–1647.
- [48] N.A. Garcia-Gomez, H.A. Mosqueda, D.I. Garcia-Gutierrez, E.M. Sanchez, Electrochemical behavior of TiO_2 /carbon dual nanofibers, *Electrochim. Acta* 116 (2014) 19–25.
- [49] W. Liao, J. Yang, H. Zhou, M. Muruganathan, Y. Zhang, Electrochemically self-doped TiO_2 nanotube arrays for efficient visible light photoelectrocatalytic degradation of contaminants, *Electrochim. Acta* 136 (2014) 310–317.
- [50] F. Hao, H. Lin, Y.Z. Liu, J.B. Li, Anionic structure-dependent photoelectrochemical responses of dye-sensitized solar cells based on a binary ionic liquid electrolyte, *Phys. Chem. Chem. Phys.* 13 (2011) 6416–6422.
- [51] Y. Rambabu, M. Jaiswal, S.C. Roy, Enhanced photoelectrochemical performance of multi-leg TiO_2 nanotubes through efficient light harvesting, *J. Phys. D: Appl. Phys.* 48 (2015) 295302.
- [52] A. Boudjemaa, S. Boumaza, M. Trari, R. Bouarab, A. Bouguelia, Physical and photoelectrochemical characterizations of α - Fe_2O_3 . Application for hydrogen production, *Int. J. Hydrog. Energy* 34 (2009) 4268–4274.
- [53] C. Odetola, L. Trevani, E.B. Easton, Enhanced activity and stability of Pt/TiO_2 /

carbon fuel cell electrocatalyst prepared using a glucose modifier, *J. Power Sources* 294 (2015) 254–263.

[54] V. Spagnol, E. Sutter, C. Debiemme-Chouvy, H. Cachet, B. Baroux, EIS study of photo-induced modifications of nano-columnar TiO_2 films, *Electrochim. Acta* 54 (2009) 1228–1232.

[55] A. Chatzitakis, A. Papaderakis, N. Karanasis, J. Georgieva, E. Pavlidou, G. Litsardakis, I. Poulios, S. Sotiropoulos, Comparison of the photoelectrochemical performance of particulate and nanotube TiO_2 photoanodes, *Catal. Today* 280 (2017) 14–20.

[56] G. Lu, A. Linsebigler, J.T. Yates, Ti^{3+} defect sites on $\text{TiO}_2(110)$: production and chemical detection of active sites, *J. Phys. Chem.* 98 (1994) 11733–11738.

[57] A.J. Bard, L.R. Faulkner, *Electrochemical Methods: Fundamentals and Applications*, 2nd ed., John Wiley & Sons Inc, 1980.

[58] H.S. Park, K.E. Kweon, H. Ye, E. Paek, G.S. Hwang, A.J. Bard, Factors in the metal doping of BiVO_4 for improved photoelectrocatalytic activity as studied by scanning electrochemical microscopy and first-principles density-functional calculation, *J. Phys. Chem. C* 115 (2011) 17870–17879.

[59] Y.R. Yang, P. Gao, X.C. Rena, L. Sha, P.P. Yang, J.J. Zhang, Y.J. Chen, L. Yang, Massive Ti^{3+} self-doped by the injected electrons from external Pt and the efficient photocatalytic hydrogen production under visible-light, *Appl. Catal. B: Environ.* 218 (2017) 751–757.

[60] M.X. Sun, X.Y. Zhang, J. Li, X.L. Cui, D.L. Sun, Y.H. Lin, Thermal formation of silicon-doped TiO_2 thin films with enhanced visible light photoelectrochemical response, *Electrochim. Commun.* 16 (2012) 26–29.

[61] V.K. Gurugubelli, S. Karmalkar, Effective medium theory of the space-charge region electrostatics of arrays of nanoscale junctions, *J. Appl. Phys.* 119 (2015) 024507.

[62] J.C. Joyner, J. Reichfield, J.A. Cowan, Factors influencing the DNA nuclease activity of iron cobalt, nickel, and copper chelates, *J. Am. Chem. Soc.* 133 (2011) 15613–15626.

[63] K. Yang, C. Meng, L.L. Lin, X.Y. Peng, X. Chen, X.X. Wang, W.X. Dai, X.Z. Fu, A heterostructured $\text{TiO}_2\text{-C}_3\text{N}_4$ support for gold catalysts: a superior preferential oxidation of CO in the presence of H_2 under visible light irradiation and without visible light irradiation, *Catal. Sci. Technol.* 6 (2016) 829–839.

[64] M.A. Butler, Photoelectrolysis and physical properties of the semiconducting electrode WO_3 , *J. Appl. Phys.* 48 (1977) 1914–1920.

[65] T. Hisatomi, J. Kubota, K. Domen, Recent advances in semiconductors for photocatalytic and photoelectrochemical water splitting, *Chem. Soc. Rev.* 43 (2014) 7520–7535.

[66] H. Park, W. Choi, Effects of TiO_2 surface fluorination on photocatalytic reactions and photoelectrochemical behaviors, *J. Phys. Chem. B* 108 (2004) 4086–4093.